ADVANCED MATERIALS

Supporting Information

for *Adv. Mater.*, DOI: 10.1002/adma.201901345

Additive Manufacturing of 3D-Architected Multifunctional Metal Oxides

Daryl W. Yee, Max L. Lifson, Bryce W. Edwards, and Julia R. Greer*

Supporting Information

Additive Manufacturing of 3D Architected Multifunctional Metal Oxides

Daryl W. Yee[†], Max L. Lifson[†], Bryce W. Edwards, Julia R. Greer*

D. W. Yee, Dr. M. L. Lifson, B. W. Edwards, Prof. J. R. Greer
Division of Engineering and Applied Science, California Institute of Technology, CA 91125, USA
E-mail: daryl@caltech.edu

Effective Two-photon Lithography Resolution

To determine the efficiency of photopolymerization via TPL, the laser was rastered between two pillars for a set number of passes at varying laser powers and raster speeds to create a test beam. It was determined that for a single raster pass, no beams could be found between the pillars. The first beam could only be observed at two raster passes, at a laser power of 50 mW and a raster speed of 100 µm/s. This beam was approximately 600 nm in width and represents the minimum size that could be achieved for a single beam. Structures that had this beam size were typically unable to survive development and would collapse on its own weight due to the poor mechanical properties of poly(ethylene glycol) diacrylate-based hydrogels. For the fabrication of sufficiently cross-linked structures, the beams had to be rastered at least 4 times at a laser power of 50 mW at a raster speed of 100 µm/s. With increased passes, the laser power and raster speed could be increased and decreased respectively. We observed a significant proximity effect (where the volume between two separate beams undergo partial polymerization due to radical diffusion) even at hatching distances of 1 µm, which results in combining of neighboring beams. In practice, this not only meant that the smallest stand-alone beams printable were of the order of 2 µm, it also meant that for sufficiently large structures with a z-layer spacing and hatching distance <600 nm, printing could still occur at lower powers and higher scan speeds since the laser was effectively rastering over the same pattern.

Two-photon Lithography Structure Writing Parameters

To determine the writing window for the photoresin, a parameter sweep was first conducted, where pillars approximately 9 µm in diameter and 10 µm tall were written with varying photon doses, at a z-layer spacing and hatching distance of 150 nm. The laser power was varied from 5 – 50 mW, in steps of 5 mW, and the laser raster speed was varied from 1 – 10 mm s^{-1}. Figure. S2 shows an SEM image of the result of the parameter sweep. As seen, a wide range of power and scan speed combinations can be used in the two-photon lithography process, due to the small z-layer spacing and hatching distances used. At the extreme ends of the power spectrum, structures were fully formed at a raster speed of 1 mm s^{-1} with a laser power of 5 mW and at 6 mm s^{-1} with a laser power of 50 mW. Regardless of power, no structures could be seen when used in conjunction with raster speeds above 6 mm s^{-1}. The parameters of 50 mW and 1 mm s^{-1} were chosen for the TPL process, as that was likely to result in the highest degree of polymer crosslinking.

Theoretical Shrinkage Calculation

The theoretical shrinkage can be determined, to a first approximation, by making the following assumptions: 1) Each mole of Zn^{2+} in the zinc-containing polymer is converted into a mole of zinc oxide (ZnO). 2) All other components in the zinc-containing polymer are removed during the combustion process, and leave no mass behind. 3) Aside from the changes in dimension from shrinkage, the net shape of the polymer is kept.

The concentration of zinc nitrate hexahydrate, c_{Zn} in the resin can be determined by:

$$c_{Zn} = \frac{m_{Zn,resin}}{V_{resin}}$$

where $m_{Zn,resin}$ is the mass of zinc nitrate hexahydrate in the prepared resin of volume V_{resin}.

For simplicity, we will print a sphere of radius $R_{printed}$ with volume $V_{printed}$. The mass, $m_{Zn,printed}$, and number of moles of zinc nitrate, $mol_{Zn,printed}$, in the printed volume, is then given by:

$$m_{Zn,printed} = c_{Zn} \times V_{printed}$$

$$mol_{Zn,printed} = \frac{m_{Zn,printed}}{Mw_{ZN}}$$

where Mw_{ZN} is the molecular weight of zinc nitrate hexahydrate.

Assuming that each mole of zinc nitrate hexahydrate is fully converted to a mole of ZnO, the number of moles of ZnO, $mol_{ZnO,printed}$, after calcination will be equivalent:

$$mol_{ZnO,printed} = mol_{Zn,printed}$$

The volume of ZnO, $V_{ZnO,printed}$ can then be determined using the bulk density, ρ_{ZnO}, and molecular weight of ZnO, Mw_{ZnO}:

$$V_{ZnO,printed} = \frac{mol_{ZnO,printed} \times Mw_{ZnO}}{\rho_{ZnO}}$$

Assuming net shape conversion, the radius of the ZnO sphere can be calculated and, the ratio of R_{ZnO} to $R_{printed}$ determined by:

$$\frac{R_{ZnO}}{R_{printed}} = \sqrt[3]{\frac{V_{ZnO,printed}}{V_{printed}}}$$

The shrinkage can then be represented by:

$$Shrinkage = \left(1 - \frac{R_{ZnO}}{R_{printed}}\right) \times 100$$

and simplified into:

$$Shrinkage = \left(1 - \sqrt[3]{\frac{m_{Zn,resin} \times Mw_{ZnO}}{V_{resin} \times Mw_{ZN} \times \rho_{ZnO}}}\right) \times 100 \qquad \textbf{[Equation S1]}$$

In this work, the zinc-containing photoresin contained 0.4 g of zinc nitrate hexahydrate in 550 µL of photoresin. The molecular weight of ZnO and zinc nitrate hexahydrate was determined to be 81.38 g/mol and 297.49 g/mol respectively. The density of bulk ZnO was taken to be 5.61 g/cm^3.[1] Using the shrinkage equation derived above, the theoretical shrinkage was determined to be 67%.

Dependence of Linear Shrinkage on Development Time

The development time of the structures in water plays a significant role in the final shrinkage observed. This is due to the fact that the zinc ions are able to diffuse out of the structure and into the surrounding water. To quantify the dependence of development time on the final linear shrinkage observed after calcination, pillars with heights of 15 µm and diameters of 9.5 µm were printed using two-photon lithography and then developed in water for varying amounts of time, followed by calcination at 500˚C. The diameters and heights of the calcined pillars were then compared against the as-printed pillars and their linear shrinkage determined via the following equation:

$$Linear\ Shrinkage = \left(1 - \frac{L_i}{L_f}\right) \times 100 \qquad \textbf{[Equation S2]}$$

where, L_i and L_f are the dimensions before and after the calcination respectively. The dependence of the linear shrinkage on development time in water is shown in Figure. S3 below.

It can be also seen that at a development time of one minute, the linear shrinkage observed was in close agreement with that determined using the analytical model described above. One minute was chosen as the shortest development time as it was the minimum amount of time needed to completely remove any uncrosslinked photoresin.

The shrinkage measurements also revealed that there was no significant anisotropy in the observed shrinkages. For each data set measured, the difference in radial and axial shrinkages, as determined by taking their absolute difference, was <2 %.

TGA

Figure. S4 shows the TGA curves of the zinc-ion containing polymer (Z2) and its corresponding zinc-free control (C1) in air. The TGA curve of Z2 showed 3 distinct stages of mass loss. At the first stage, from 30 – 115˚C, 16 wt% of mass loss was observed. This corresponds to the mass loss associated with the evaporation of water. From 115 – 150˚C, a rapid mass loss of approximately 50% was observed, which corresponds to the combustion process from the interaction between the nitrates and PEGda. Above 150˚C, a slow decomposition corresponding to a mass loss of 16% was observed, indicating the elimination of any residue organic material left behind from incomplete combustion. Beyond 400˚C, no further mass loss was observed. On the other hand, the TGA curve of C1 showed a different thermal behavior. From 30 – 100˚C, a large mass loss of 50% was observed, due to the loss of water from the polymer. No change in mass was observed from 100 – 170˚C as the PEG was stable in that temperature range. On further heating to 400˚C, the polymer then underwent a gradual mass loss of ~40 wt%, and then completely degraded past 500˚C. The two drastically different TGA curves is a clear demonstration of the influence of the metal nitrate salt during the calcination process.

In situ Electromechanical Experiment

Figure. S7 illustrates the electromechanical experimental setup. The sample is mounted onto an aluminum SEM stub using colloidal graphite (Ted Pella, Inc.), which is then mounted into a 90° SEM cube. This is attached to the stage such that the electron beam is viewing the cross section of the sample. The conductive flat punch tip is attached to the extension arm of the nanomechanical indenter, which can be finely controlled. Two coax cables are attached to an electrical port on the SEM chamber. The external cables are connected to the potentiostat. The internal coax cables are each split into a conduction wire and a shielding wire, each ending with an alligator clip. Both shielding wires are attached to the sample stage, which is connected to ground through the SEM door. One conduction wire is attached to the tip and the other is attached to the stage, to attempt to hold one side of the measurement to ground. The tip can now be moved to the top of the sample under test using the sample stage and extension arm linear motor. This is configured so that the experiment is centered under the electron beam.

A typical compression test would proceed as follows: An image is taken before any displacement is applied. The e-beam and CCD camera are turned off. An OCV measurement is started on the potentiostat. With no additional stimulus, this results in a long term decaying voltage response, as seen in Figure. S9. This response is likely due to the charge built up during imaging dissipating within the complicated system. After several seconds, the extension arm linear motor is given a command to move a specified number of microsteps, which are fractions of a revolution of the motor. When the sample exhibits an electromechanical response, this sudden displacement correlates to a sudden change in the voltage; in this case the drop in voltage indicates negative charge has been induced. Due to the large RC constant of the system, the background electrical response over the relatively short and consistent experiment time, typically 20 seconds after waiting 10-60 seconds after beginning the OCV measurement, can be treated as linear. This voltage change from the typical decay behavior can be identified and measured via MATLAB code. After several additional seconds, the OCV measurement is stopped, the e-beam is turned back on, and an image is taken. The difference between this image and the one taken before the compression can be used to accurately measure the applied displacement. If the sample remains intact, another measurement can be taken in a similar manner. Electrical data presented is always from at least the second measurement on each sample to ensure complete contact with the sample and to avoid any sudden (or difficult to reproduce) mechanical and electrical shocks to the system. In order to perform the experiment on the next sample, the tip displacement is reset and the sample stage is repositioned to the new location.

In-situ Electromechanical Circuit Analysis

In order to place the measured electromechanical response in the context of the expected measurement circuit, a Simulation Program with Integrated Circuit Emphasis, or SPICE, model was created in Ltspice XVII (Analog Devices, Inc.), using a simplified equivalent circuit. A graphical representation of this model can be found in Figure. S10. The wire from the potentiostat and the aluminum stub it is connected to will have a small resistance and capacitance value. The tungsten carbide (WC) tip not only has a resistance and capacitance associated with the material itself, it also has a resistance and capacitance of contact. As a simplification of this system, these values can be combined into a generalized tip resistance R_c and capacitance C_c, respectively. By placing the WC tip in contact with the aluminum SEM stub and calculating the slope of a measured I-V curve, we can estimate a rough value

for the combined resistance of the circuit from these components, which are contained in the terms R_c and R_w, where R_w is the resistance of the SEM stub to the potentiostat lead. The I-V curves for these measurements are all linear in this work, indicating ohmic behavior. The value for this combined term was measured as 64 kΩ. Using a simple ohmmeter, we measured R_w, to be approximately 4 Ω. Therefore, since these components are in series, we assume a value of 64 kΩ for R_c. In order to account for the resistance of the Si substrate, R_b, the tip was placed in contact with the Si surface adjacent to a sample of interest and an I-V curve measurement was taken. This resulted in a total resistance of 168 kΩ. Since R_b is in series with R_c and R_w, we estimate R_b to be 104 kΩ. R_b and C_b include the resistance and capacitance of contact and assumes that the value between the WC tip and Si substrate is similar to that between our material and the Si substrate. During the experiment, the tip is in contact with the sample of interest, in this case the ZnO tetrakaidecahedron unit cell, which will have a resistance R_s and capacitance C_s. It is on this capacitor C_s that charge will accumulate via the piezoelectric effect when stress is applied to the sample. The value of R_s will be discussed shortly. The voltage measured during the open circuit voltage experiment is V_m. For this equivalent circuit model, we assume that the inductance of the components will have a minimal effect on the reactance.

In order to simply simulate the electromechanical response of our sample, we have included a voltage source, V_s, in parallel with the capacitor C_s. We have also included a measurement isolation resistance R_m and capacitance C_m that sit between the measurement point V_m and ground. These values have been reported by the potentiostat manufacturer as 10 MΩ and 10 nF, respectively. Since we are performing a DC operating point simulation, creating a purely DC voltage-based illustration, we have defined all other capacitances as 10 pF. Since these capacitors are treated as shorts by this model, we are also assuming the charges that are built up during imaging are negligible on the behavior of C_s and V_m. By setting V_s equal to 1 V, V_m in the model shows us the factor by which the measured voltage is reduced and $1/V_m$ shows us the multiplicative factor to convert our measured voltage to an estimated sample voltage.

Before calculating V_m, we need to first determine R_s. Since the exact conductive pathway of the final architecture and the resistivity of our constituent material is not known, we assume initial values for these parameters and examine the sensitivity of our circuit model to R_s. As our initial starting point, Roy et al. have shown that the room temperature resistivity of ZnO pellets made from compressed powder with an average initial grain size of 80 nm is 0.75 M Ωm.[2] For the conductive pathway, the tetrakaidecahedron unit cell beam diameter is 830 nm and the structure is 5.6 μm tall. As a simplification, if we envision this structure as a single cylinder with these diameter and height values, we can estimate the resistance of this object by using: $R = \rho(L/A)$, where ρ is the material resistivity, L is the length of the object, and A is the cross-sectional area of the object.[3] Using our assumed values, this leads to an R_s of 7.8×10^{15} Ω. When the simulation is run with these values and V_s = 1 V, it results in V_m = 0.983 V. This means that the measured voltage is practically equal to the voltage generated by the sample, given our model assumptions. In fact, due to the layout of the circuit, V_m appears to not be sensitive to R_s when spanning up and down 4 orders of magnitude. By contrast, V_m drops to 0.901 and 0.489 when R_b is increased by one and two orders of magnitude, respectively. The system response is similarly sensitive to increases in R_c and decreases in R_m. Further understanding of the microstructure is required to fully model the electrical and mechanical response of the material, which could then enable true 3D finite element analysis modeling, avoiding many of the simplistic assumptions made for this proof of concept demonstration.

Mechanical compression experiments on the ZnO tetrakaidecahedrons

We performed quasi-static compressions of individual ZnO tetrakaidecahedron unit cells to determine the structural loading stiffness using an in situ nanoindenter (InSEM by Nanomechanics) at a strain rate of 10^{-3} s^{-1}. For the cyclic compression experiment, a structure was subjected to 9 cycles of uniaxial compression of 200 nm. The load-displacement curves are shown in Figure. S12. The loading stiffness was calculated by taking the slope of the load-displacement curves between 150 and 190 nm. The unloading stiffness was calculated by taking the slope of the load-displacement curves between 185 and 145 nm. A video of the cyclic displacement experiment is also included in the Supporting Information. The structure was then compressed to failure in a separate experiment.

A moving average filter was applied to the cyclic load-displacement data to reduce noise and ease visualization of each cycle preformed. A linear correlation between cumulative error and filter size was observed, so we chose the smallest filter that allowed us to more easily see the trends in the data. The filter size turned out to be 10 data points in this case. The filter was applied using the cumulative sum function found in the Numpy package of Python. There are 46,000 total data points in this set.

To determine the loading stiffness of the ZnO tetrakaidecahedron unit cells that were tested to failure, we measured the slope of the load-displacement curves between 150 and 190nm in Figure. S11. We chose these values so that we could compare both the cyclic test and the tests to failure under the same displacement range, which should correspond to the same strain, as these unit cells are approximately the same size. The average stiffness was determined to be 2.19 ± 0.20 kN/m.

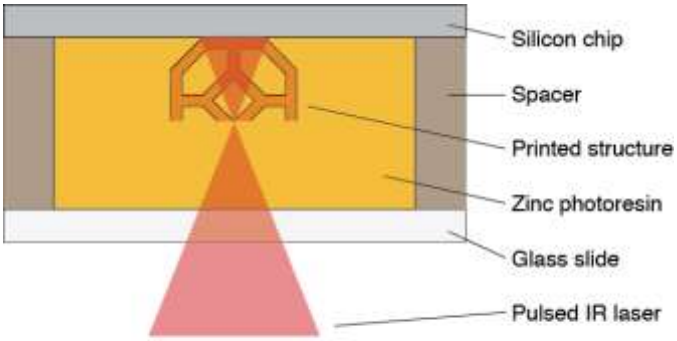

Figure S1. Schematic of the two-photon lithography set-up. Kapton tape approximately 100 µm thick was used as spacers between the silicon chip and the glass slide. The structures were written using two-photon lithography on the silicon chip and written down towards the glass slide.

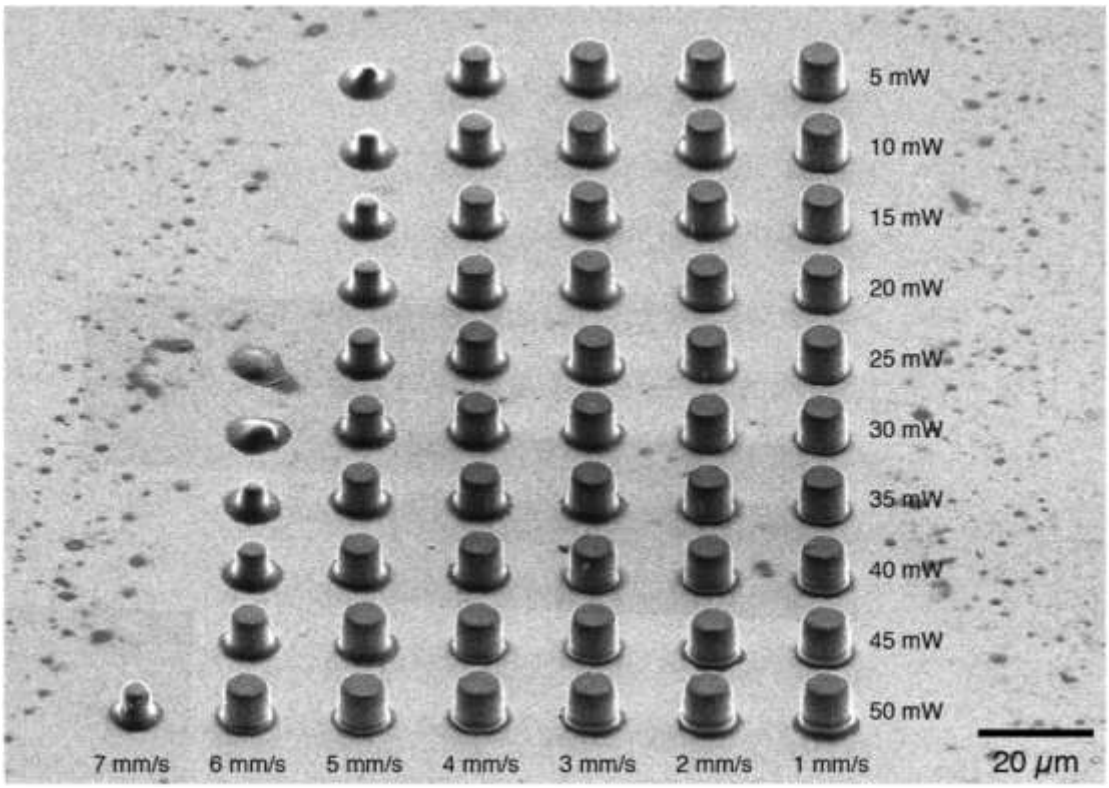

Figure S2. Two-photon lithography write parameter sweep. To determine the polymerization window of the zinc-ion containing photoresin, pillars 9 µm in diameter and 10 µm in height were written with varying laser powers and laser scan speed. The laser power was varied from 5 – 50 mW in steps of 5 mW, and the scan speed was varied from 1 – 10 mm s^{-1}, in steps of 1 mm s^{-1}.

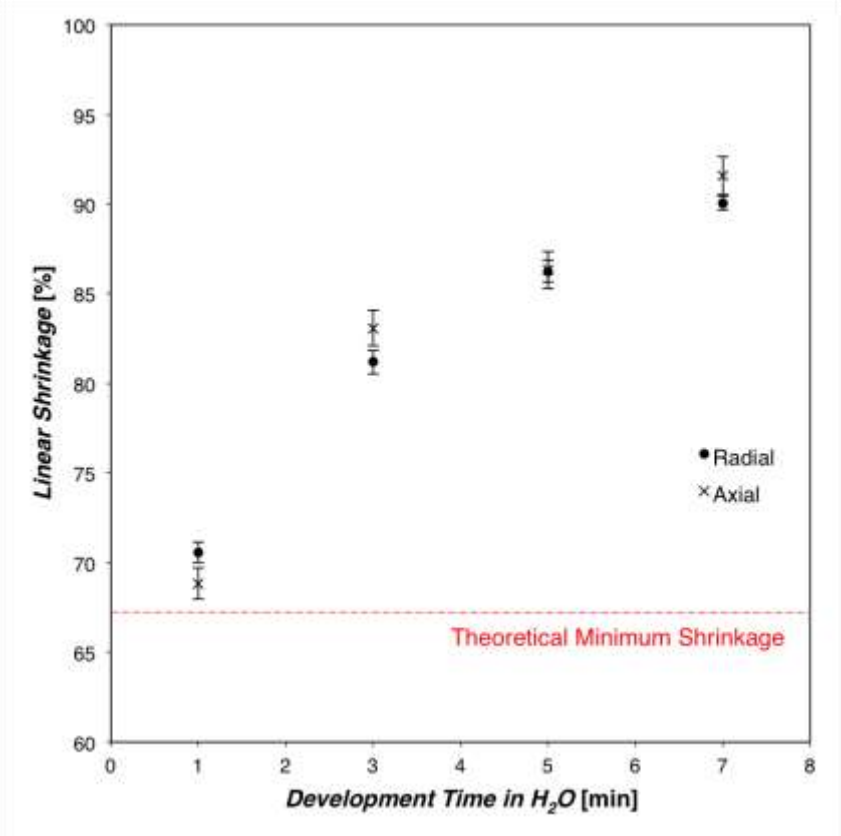

Figure S3. The dependence of linear shrinkage of development time in water. A positive correlation between the development time and linear shrinkage can be observed. This is due to the zinc ions leaching into the water over time, resulting in a loss of zinc in the structure, and consequently the volume of zinc remaining after calcination. The linear shrinkage after one minute of development resulted in linear shrinkages that were in close agreement with that predicted using the analytical model described above. Comparison of the radial and axial shrinkages showed that there was no significant anisotropy in the observed shrinkages.

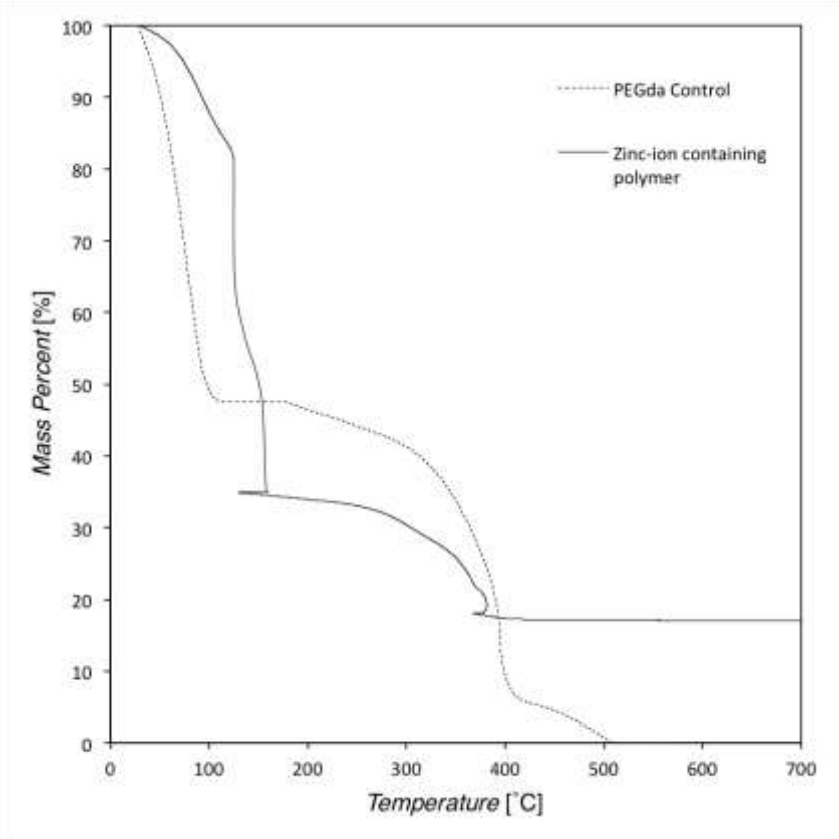

Figure S4. Thermogravimetric analysis of the zinc-nitrate containing polymer and its control. TGA data of polymers prepared from photoresin Z2 and C1. A rapid mass loss from 115 – 150˚C can be observed with the zinc-nitrate containing polymer, which is absent in the control sample. The large mass loss in the control polymer on heating to 100˚C is due to the loss of water in the polymer. This is clear evidence of the combustion process from the ignition of the zinc nitrate oxidizer and the polymer. The control also exhibits complete mass loss above 500˚C, whereas ZnO remains behind from the Z2 photoresin.

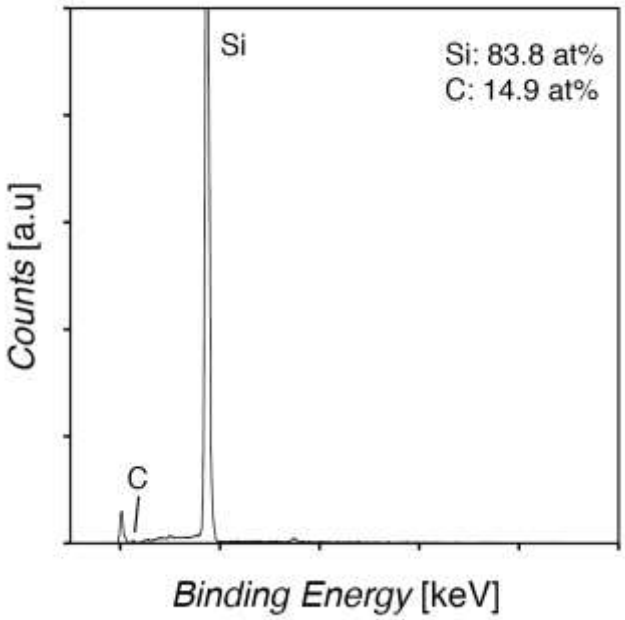

Figure S5. EDS composition spectrum of Si substrate**.** A large amount of carbon can be detected on the Si substrate after calcination. It is possible that the high amount of carbon detected is due to organic reside left behind during the combustion process or from the SEM chamber itself.

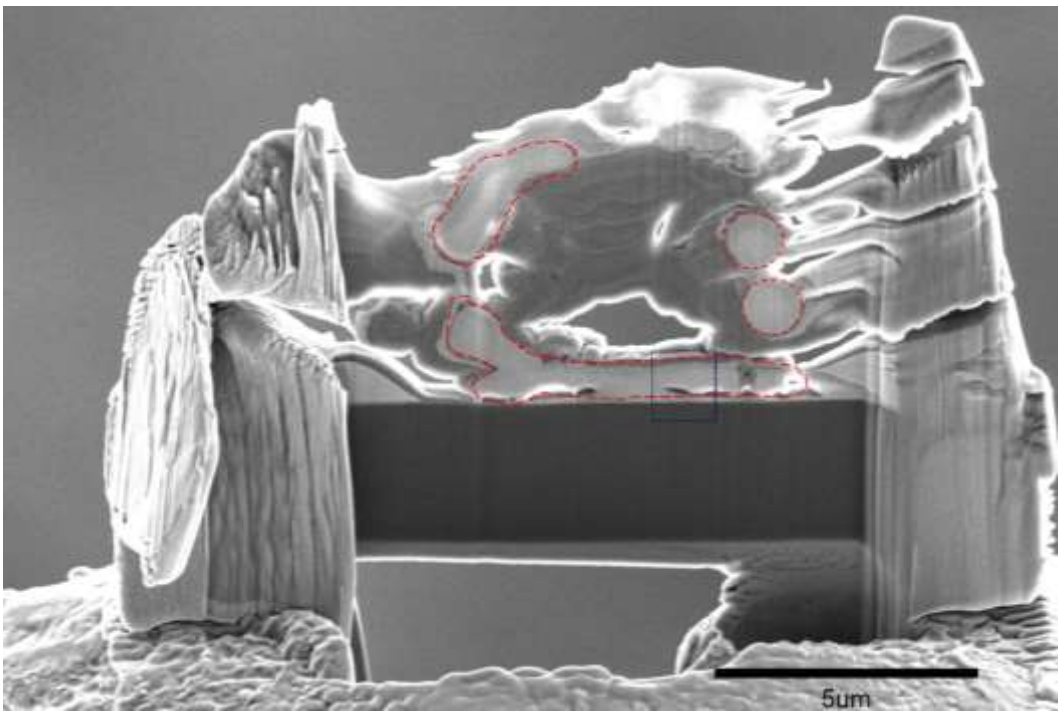

Figure S6. FIB cross section liftout of tetrakaidecahedron unit cell on Si for TEM analysis. Cross-section SEM image of the FIB liftout, with deposited Pt protection before final thinning. The red dashed shapes represent the captured sections of the unit cell beams. The blue dotted box indicates the area of TEM analysis, as it provided the thinnest cross section within the sample.

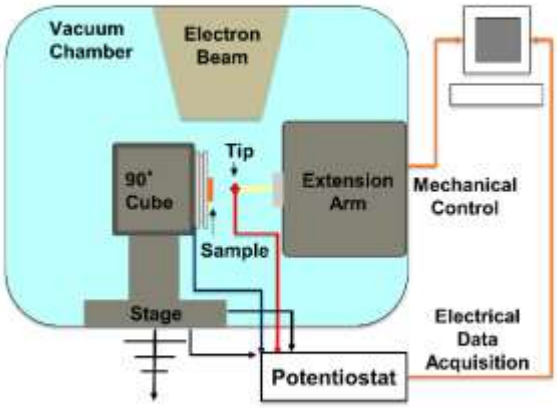

Figure S7. Schematic of the electromechanical experimental setup. The sample is placed on an aluminum stub, mounted at 90°, in an SEM chamber equipped with a nanoindenter arm. A potentiostat is connected to measure the open circuit voltage between the grounded stage and the indenter tip during the experiment.

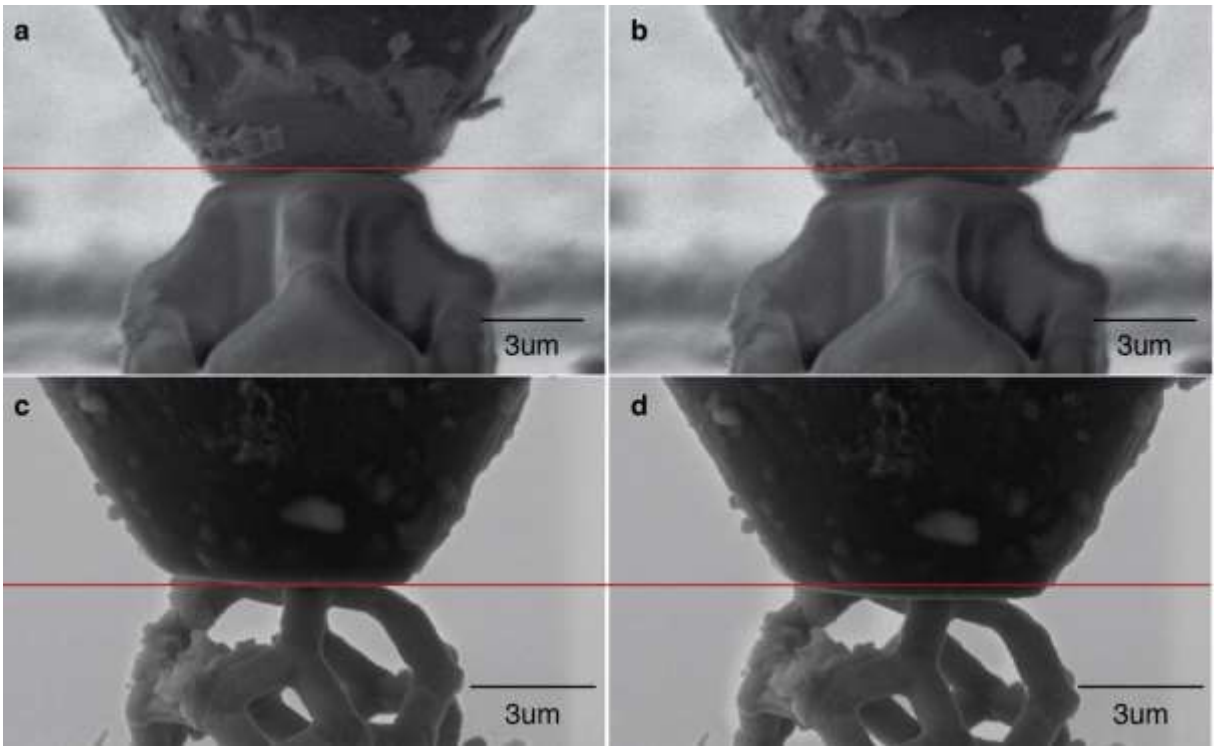

Figure S8. Magnified SEM images of the compression. Compression of the zinc-ion containing polymer tetrakaidecahedron structure a) before and b) after 350 nm of displacement. Compression of the ZnO tetrakaidecahedron structure c) before and d) after 200 nm of displacement. The red line serves as a guide to the eye in both sets of images.

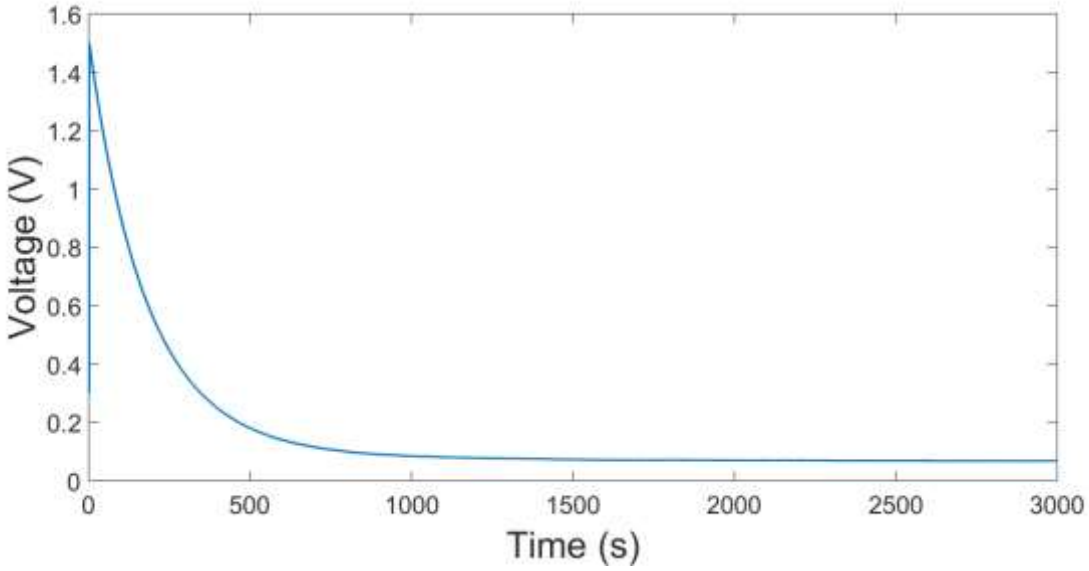

Figure S9. Long term open circuit voltage response of the measurement system during electrical experiment. Voltage versus time behavior of the measurement system when in contact with a sample, but no displacement is applied. The initial charge, likely built up from imaging with the electron beam, slowly discharges to a steady state value.

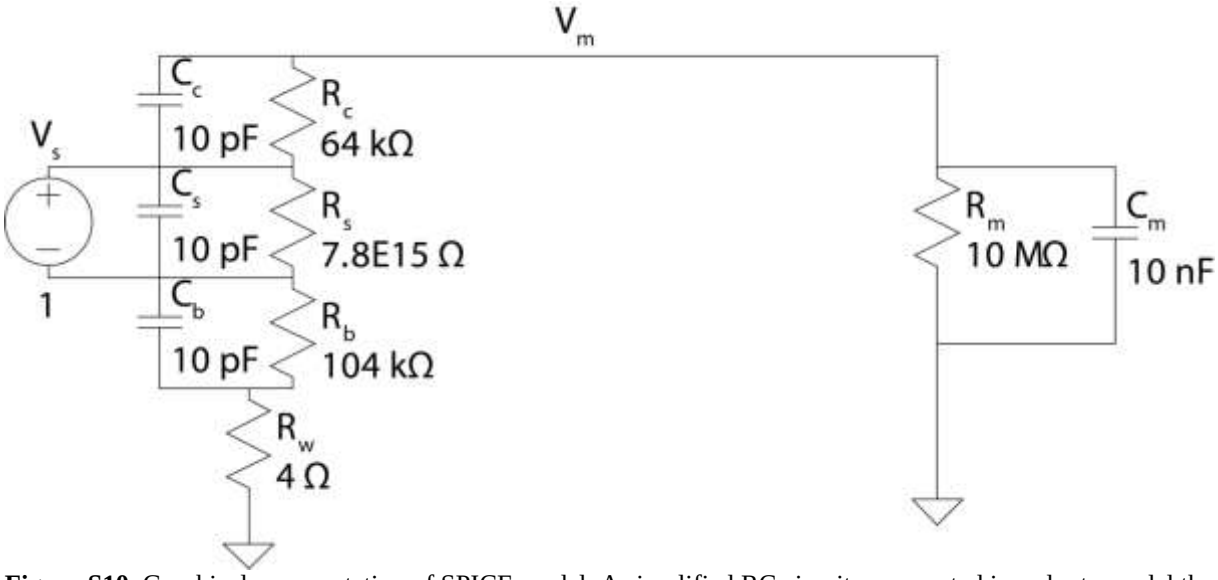

Figure S10. Graphical representation of SPICE model. A simplified RC circuit was created in order to model the relationship between the measured voltage and the voltage generated by the sample. R_m and C_m represent the isolation resistance and capacitance of the potentiostat, respectively, while V_m represents the voltage measured by the potentiostat. R_c and C_c, R_s and C_s, and R_b and C_b represent the resistance and capacitance of the tip, the sample, and the substrate, respectively. R_w represents the resistance of the pathway from the SEM stub to the potentiostat. V_s is placed in parallel with the capacitor C_s and is a simplified representation of the voltage generated by the applied displacement.

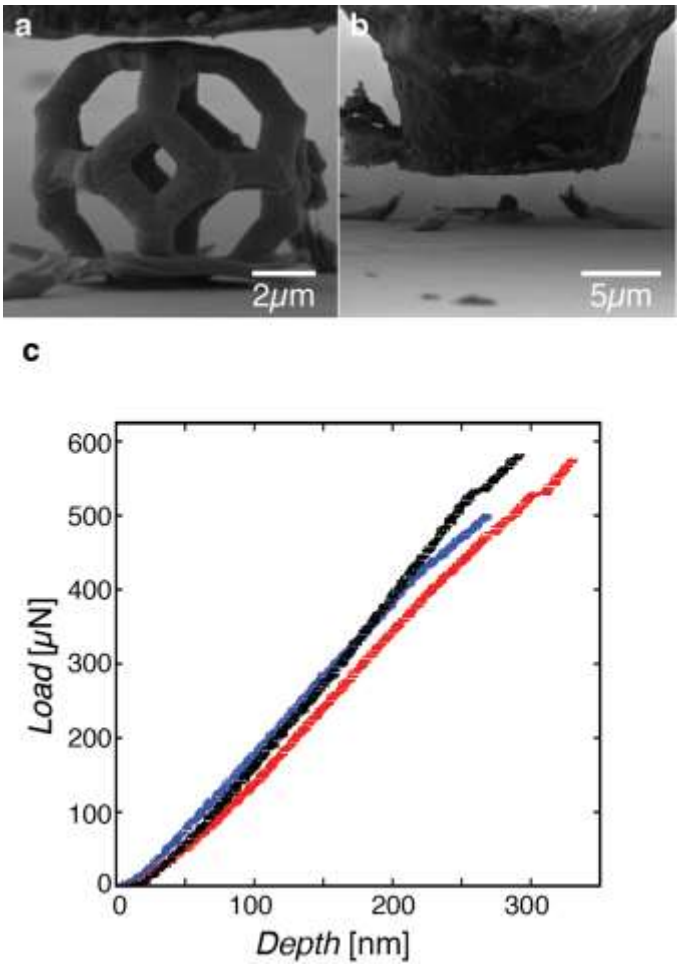

Figure S11. Uniaxial compression experiments on the ZnO tetrakaidecahedrons. SEM images of the ZnO structure a) before and b) after compression to failure. c) Analysis of the load – displacement curves of three separate ZnO structures compressed to failure indicated that the structures had an average stiffness of 2.19 ± 0.20 kN/m. The structure given by the black line underwent 9 cycles of compression to 200 nm prior to compression to failure. The average displacement to failure was 294 ± 25 nm, representing a compressive strain to failure of ~3.5%.

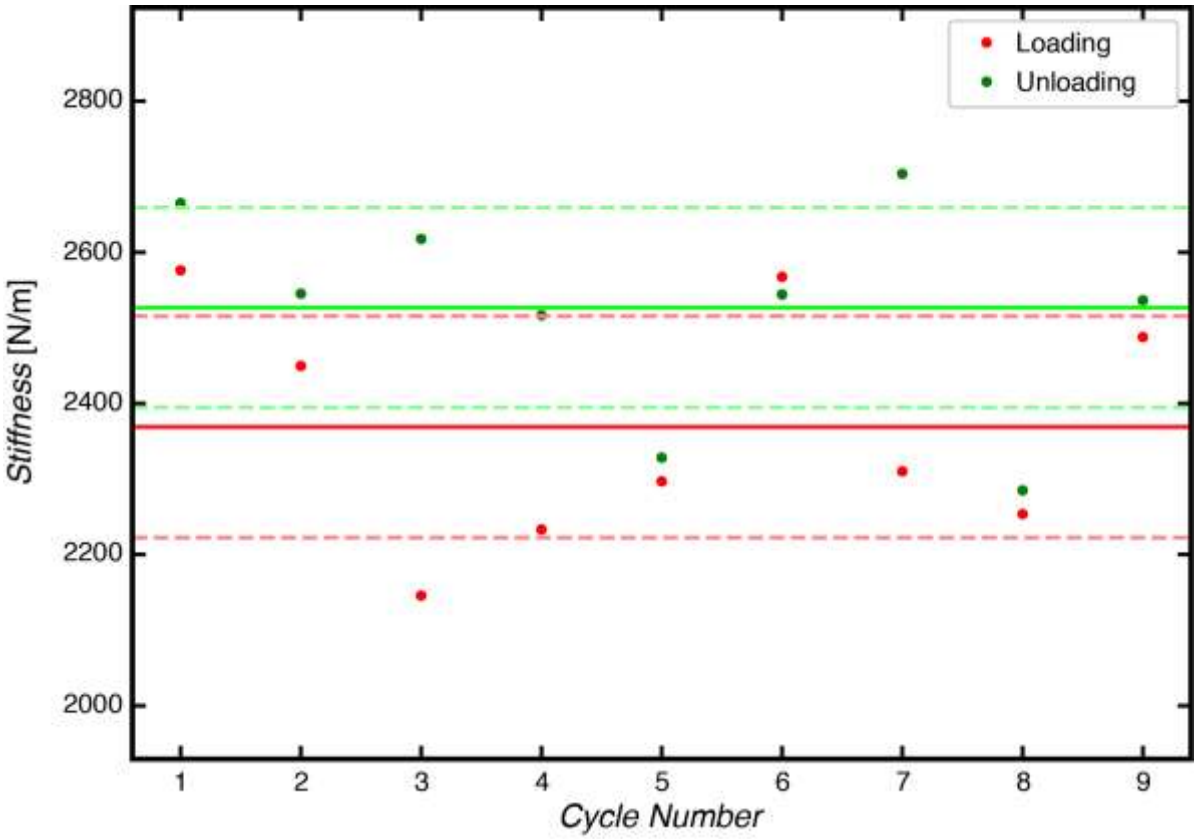

Figure S12. Loading and unloading stiffness measurements of a single ZnO tetrakaidecahedron structure over 9 cycles of compression. The solid line represents the average value and the dashed lines are one standard deviation away from that. The average loading and unloading stiffness over the 9 cycles was 2.37 ± 0.15 kN/m and 2.52 ± 0.13 kN/m. respectively No discernible trends in stiffness were observed over the 9 cycles of compression. The sample was then compressed to failure and the measured loading stiffness was determined to be 2.46 kN/m.

Table S1: Linear shrinkage after heat treatment

Structure	Initial Width [µm]	Final Width [µm]	Linear Shrinkage
Pillar	7.38	1.08	85.3%
Tetrakaidecahedron Unit Cell	41.70	6.12	85.3%
2x2 Tetrakaidecahedron Lattice	55.00	5.92	89.2%

References

[1] J. Hu, R. G. Gordon, *J. Appl. Phys.* **1992**. 72, 5381.

[2] T. K. Roy, D. Sanyal, D. Bhowmick, A. Chakrabarti, *Mater. Sci. Semicond. Process.* **2013**, 16, 332.

[3] C. K. Alexander, M. N. O. Sadiku, *Fundamentals of Electric Circuits*, McGraw-Hill, New York, NY, USA **2009**.